Geochimica et Cosmochimica Acta 414 (2026) 134–145

Contents lists available at ScienceDirect

Geochimica et Cosmochimica Acta

journal homepage: www.elsevier.com/locate/gca

Quantifying contributions of iron (oxyhydr)oxides and organic matter to chromium dynamics in paddy soils

Guojun Chen [a,b,1], Yang Yang [b,1], Ke Zhang [b], Yan Ru [b,c], Zebin Hong [b], Xiaomin Li [d], Taicheng An [a], Pei Wang [e], Songxiong Zhong [b], Qi Wang [b], Shiwen Hu [b], Fangbai Li [b], Tongxu Liu [b,*]

[a] Guangdong Key Laboratory of Environmental Catalysis and Health Risk Control, School of Environmental Science and Engineering, Institute of Environmental Health and Pollution Control, Guangdong University of Technology, Guangzhou 510006, China
[b] National-Regional Joint Engineering Research Center for Soil Pollution Control and Remediation in South China, Guangdong Key Laboratory of Integrated Agro-environmental Pollution Control and Management, Institute of Eco-environmental and Soil Sciences, Guangdong Academy of Sciences, Guangzhou 510650, China
[c] Fujian Provincial Key Laboratory of Soil Environmental Health and Regulation, College of Resources and Environment, Fujian Agriculture and Forestry University, Fuzhou, Fujian 350002, China
[d] SCNU Environmental Research Institute, Guangdong Provincial Key Laboratory of Chemical Pollution and Environmental Safety & MOE Key Laboratory of Theoretical Chemistry of Environment, South China Normal University, Guangzhou 510006, China
[e] School of Tropical Agriculture and Forestry, Hainan University, Haikou 570228, China

ARTICLE INFO

Associate Editor: Mlanie Davranche

Keywords:
Chromium
Fe (oxyhydr)oxides
Organic matter
Soils
Modeling

ABSTRACT

Basalt-derived paddy soils contain high concentrations of chromium (Cr) from basalt weathering. Considering the potential risks of available Cr to human health, the transformation of Cr in basalt-derived paddy soils has attracted worldwide attention. However, the mechanisms controlling the biogeochemical cycling of Cr in these soils remain unclear. Here, pot experiments were performed to investigate Cr migration and transformation throughout the flooding–drainage cycle. The dynamic changes in soil chemical (e.g., dissolved organic carbon (DOC), iron (Fe) (oxyhydr)oxides, sulfate, and nitrogen (N) species) and physical properties (e.g., UV–vis spectra, pore size distribution, and surface site concentrations) were investigated. The available Cr increased during flooding and decreased during drainage. Cr concentrations in rice grains exceeded the safety threshold, indicating high Cr availability in these soils and the associated risk to human health. A kinetic model was developed to unravel the key factors controlling Cr transformation. During flooding, the mobilization of the available Cr was primarily driven by Fe (oxyhydr)oxides (76.4%), with a smaller contribution from organic matter (OM) (23.6%). During drainage, the sequestration of the available Cr was similarly dominated by Fe (oxyhydr)oxides (76.6%), followed by OM (23.4%). Furthermore, within the Fe (oxyhydr)oxides, metastable Fe phases played a predominant role in the available Cr immobilization (accounting for 91.6% of the total Fe contribution), while stable Fe phases contributed the remaining 8.4%. These insights are vital for understanding Cr mobility and availability in paddy soils with a high geological background.

1. Introduction

Chromium (Cr) contamination is prevalent, originating from both geological processes and human activities (Novak et al., 2017). In paddy soils, Cr(III) and Cr(VI) are the two primary oxidation states (Chen et al., 2019a). Previous studies on Cr transformation in paddy soils predominantly focused on Cr(VI), which is usually associated with human activities (Liu et al., 2024; Wang et al., 2024; Xiao et al., 2021; Yang et al., 2022; Zhang et al., 2022). Prolonged flooding creates highly reducing conditions that favor the dominance of Cr(III) in paddy soils (Li et al., 2024). The mechanism of geogenic Cr(III) migration and transformation in paddy soils remains poorly understood. Although less toxic than Cr (VI), high levels of Cr(III) severely affect the rice plant growth, reduce rice production, and pose health risks (Ertani et al., 2017). Basalt weathering is an important geogenic Cr source, contributing to high Cr accumulation in paddy soils (Wang et al., 2020). Cr mobility and

* Corresponding author.
E-mail address: txliu@soil.gd.cn (T. Liu).
[1] These authors contributed equally to this work.

https://doi.org/10.1016/j.gca.2025.12.050
Received 29 May 2025; Accepted 22 December 2025
Available online 23 December 2025

availability are crucial factors influencing Cr accumulation in rice (Ao et al., 2022). Therefore, a better understanding of Cr(III) mobility and availability in soil-rice plant systems is essential.

Rice, a vital staple for many Asian populations, is grown under alternating flooding and drainage conditions (Wiggenhauser et al., 2021). These conditions significantly impact the redox status of paddy soils and the biogeochemical cycles of iron (Fe) and carbon (C) (Huang et al., 2023). Fe redox transformations strongly influence the mobility of co-existing metals in paddy soils (Yu et al., 2016). Flooding induces reducing conditions, under which Cr could be released through reductive dissolution of Fe (oxyhydr)oxides (Davranche and Bollinger, 2000). Reduction of Fe(III), nitrate, and sulfate consumes protons, thereby elevating pH and decreasing the positive charge on soil surfaces via deprotonation (Lu et al., 2023). This can promote partial Cr resorption onto soil particles or residual Fe (oxyhydr)oxides. Soil organic matter (OM) may affect Cr mobility as well (Liu et al., 2019). Soil OM can adsorb onto Fe (oxyhydr)oxides, forming OM–Fe oxide complexes (Dong et al., 2023). Reduction of Fe (oxyhydr)oxides liberates dissolved organic matter (DOM) during flooding (Song et al., 2022). DOM represents the most reactive fraction of soil OM (Santos et al., 2024). With numerous active functional groups, DOM forms complexes with Cr and potentially increases Cr mobility (Liu et al., 2019; Kelly et al., 2020).

Following drainage, these trends were reversed (Huang et al., 2023). Fe(II) was oxidized to newly formed Fe(III) minerals, which serve as prevalent adsorbents (Chen et al., 2023; Chen et al., 2021). Consequently, Cr may be immobilized by both metastable and stable Fe (oxyhydr)oxides (Hu et al., 2024). In the case of metastable Fe (oxyhydr) oxides, Cr can be retained through surface adsorption or physical encapsulation, leading to the formation of co-precipitates. In the case of stable Fe (oxyhydr)oxides, Cr may be transferred into the residual fraction through lattice incorporation or occlusion within the crystalline structure. OM could immobilize Cr(III) on soil particle surfaces via physical adsorption or chemical bonding (Ao et al., 2022; Ohta et al., 2012). The oxidation of Fe(II), nitrite, and sulfite leads to a substantial release of protons and a significant decrease in pH (Chi et al., 2023). These protons compete with metal cations for adsorption sites (Chi et al., 2023), potentially desorbing Cr from Fe (oxyhydr)oxides and OM (Ma and Hooda, 2010). The bidirectional transformation of Cr, where Cr is both released and subsequently re-fixed by Fe (oxyhydr)oxides and OM, makes it challenging to identify the key processes controlling Cr dynamics and to quantify the contributions of Fe (oxyhydr)oxides and OM.

To address these challenges, kinetic models offer a valuable tool. Unlike traditional fractionation analyses, kinetic modeling can quantify the rates and relative contributions of mobilization and sequestration processes, providing a dynamic understanding of Cr behavior under fluctuating redox conditions. Recent studies have employed kinetic models to evaluate temporal changes in different fractions of heavy metals [e.g., lead (Pb), nickel (Ni), and cadmium (Cd)] (Huang et al., 2023; Lu et al., 2023; Yang et al., 2021). The relative contributions of key factors to the mobilization and sequestration of heavy metals throughout the flooding–drainage cycle have not been quantified.

Flooding-drainage cycles may continuously influence Cr accumulation in rice grains. The safety threshold for Cr in rice grains is 1.0 mg/kg (Ali et al., 2022). Rice plants are highly efficient in Cr uptake, transport, and accumulation (Satpathy et al., 2014). Cr(III) uptake and transport in rice plants are likely mediated by passive mechanisms (Ali et al., 2020). Observing changes in Cr concentrations in rice grains throughout the flooding–drainage cycle provides direct evidence of variations in Cr availability in paddy soils.

In this study, pot experiments were conducted using basalt-derived paddy soil containing 288 mg/kg Cr. The specific objectives of this study were to: (i) explore Cr availability in soil and Cr accumulation in rice during the flooding-drainage process; (ii) quantify the relative contributions of Fe (oxyhydr)oxides and OM to Cr transformation under flooding and drainage conditions in soils. This study contributes to enhancing the quantitative understanding of Cr biogeochemical cycling in basalt-derived paddy soils.

Table 1
Physicochemical properties of the paddy soil. CEC represents cation exchange capacity; SSA represents specific surface area.

Parameters	Units	Paddy soil
CEC	(cmol/kg)	11.8
Organic matter	(g/kg)	29.2
Carbonate	(g/kg)	0.25
SSA	(m^2/g)	26.2
Total Fe	(g/kg)	86.5
Total Mn	(g/kg)	0.45
Total Cr	(mg/kg)	288
Total P	(g/kg)	0.9
Sand	(g/kg)	161
Silt	(g/kg)	318
Clay	(g/kg)	521

2. Materials and methods

2.1. Soil characterization

Surface soil samples from depths of 0–20 cm were obtained from Leizhou Peninsula in Zhanjiang City, Guangdong Province, China. The soils were air-dried, sieved through a 2 mm mesh, and stored in plastic containers for analysis. The physicochemical properties, including cation exchange capacity (CEC), OM content, carbonate, specific surface area (SSA), total Fe, Mn, P, and Cr concentrations, and soil texture (sand, silt, and clay), were measured (Table 1, Text S1 of Supplementary material).

2.2. Pot experiments

Uniformly sized rice seeds (Nipponbare, *Oryza sativa* L. japonica) were chosen and disinfected with 30 % H_2O_2 for 15 min. Then the rice seeds were rinsed with deionized water (< 0.1 μs cm^{-1}), germinated in liquid nutrient solutions at 25 ℃, and irradiated with artificial light (70 μmol/m^2·s for 12 h during daytime and 12 h dark period). After four weeks of growth, uniformly sized seedlings were chosen and transplanted to each pot with 5 kg of dry soil in a greenhouse. The rice plants were irrigated for 80 d by maintaining water depth of above 5 cm on the soil surface, followed by drainage management for 15 d by maintaining 70 % of the water content. Urea was utilized at a rate of 187.5 kg N/ha (Xiao et al., 2015). KCl and KH_2PO_4 were applied as basal fertilizer. A total of 18 pots were set for the pot experiment, and triplicate pots was sampled during flooding and drainage. After harvesting, the plants were divided into root, straw, and grain fractions.

2.3. Paddy soil and rice plant sample analysis

The pH and Eh values were monitored *in situ* by a pH electrode and a Pt combined electrode (Mettler Toledo, Switzerland), respectively. Soil porewater was collected with the core water sampler (Rhizon MOM, Netherlands) and filtered with a filter of 0.45 μm. Ion chromatography was used to measure concentrations of NO_3^- and SO_4^{2-}. Fe speciation was extracted from 0.7 g of solid-phase sample using 0.5 M HCl. The measurements of dissolved Fe(II) ($Fe(II)_{dissolved}$), HCl-extractable Fe(II) and Fe(III), ($Fe(II)_{HCl}$ and $Fe(III)_{HCl}$) and DOC were further detailed in Text S2 of Supplementary material. The Cr fractions including exchangeable Cr (F1), carbonate-bound Cr (F2), Fe–Mn oxide-bound Cr (F3), OM-sulfide-bound Cr (F4), and residual Cr (F5) in the soil were characterized using the five-step Tessier sequential method (Tessier et al., 1979). The concentrations of Cr(VI) in Cr fractions (F1, F2, F3, and F4), as well as dissolved Cr in porewater (F0), were measured using the diphenylcarbazide method (Chen et al., 2019b). Cr(VI) was not detected throughout the experiments. Total Cr concentrations in the solutions

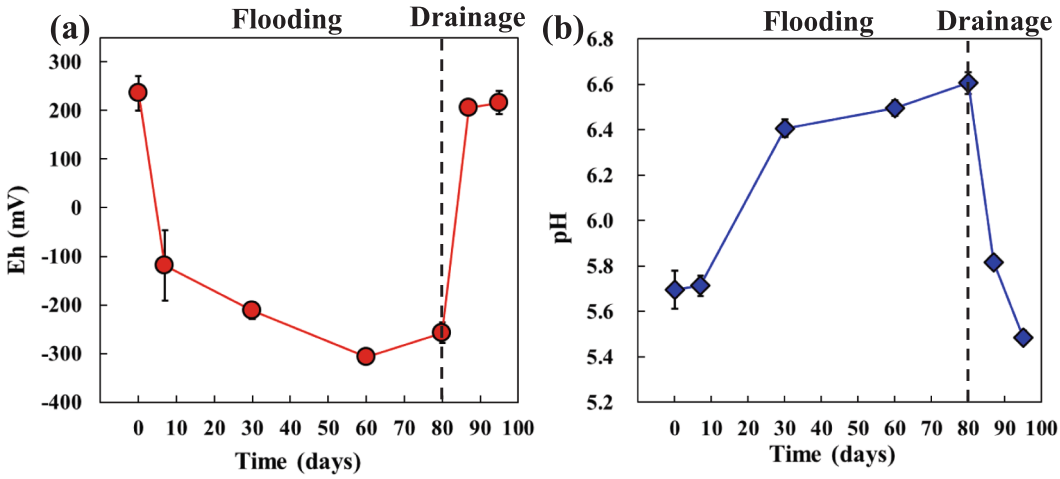

Fig. 1. Changes in soil Eh (a) and pH (b) throughout the flooding and drainage cycle. The dashed line indicates the transition from flooding to drainage.

were measured by ICP-OES.

UV–vis spectrophotometry was used to measure the colloids released in the supernatant during flooding (0 and 80 d) and drainage (95 d). The unfiltered samples were centrifuged at 5000 rpm for 10 min to remove large suspended particles, enhancing the optical response of soil colloids, and then scanned between 200 and 600 nm. Pore structure characterization of soil samples collected on 0 d, 80 d, and 95 d was performed using mercury intrusion porosimetry (MIP) (AutoPore IV 9500, Micromeritics, USA). The continuous potentiometric titrations of the soil samples were carried out through the flooding-drainage cycle. The autotitrator (905 Titrando, Metrohm, Switzerland) and the Gran plot method were used to determine the surface site concentration (H_s) (Lu et al., 2023). The details of measurements of the surface site concentration were provided in Text S3 of Supplementary material. Two

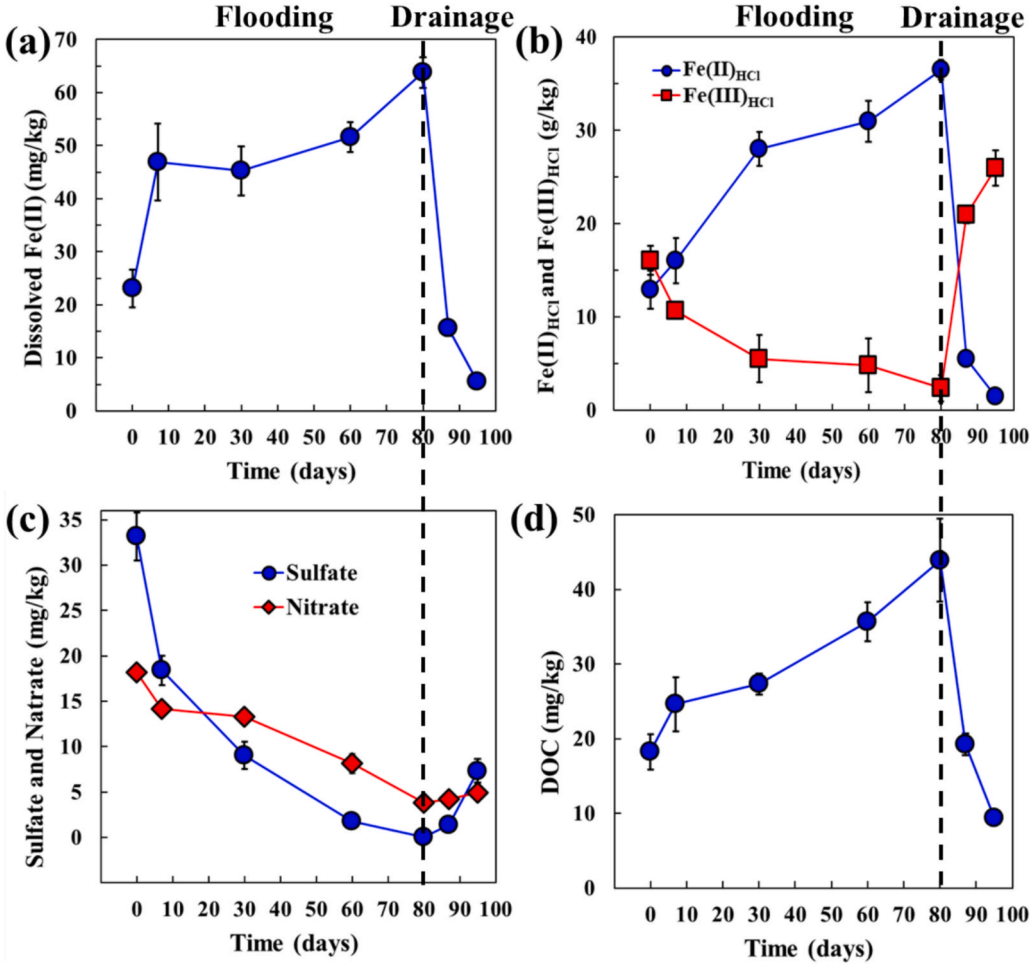

Fig. 2. Concentrations of dissolved Fe(II) (a), HCl-extractable Fe(II) ($Fe(II)_{HCl}$) and HCl-extractable Fe(III) ($Fe(III)_{HCl}$) (b), sulfate and nitrate (c), dissolved organic carbon (DOC) (d) throughout the flooding and drainage cycle. The dashed line indicates the transition from flooding to drainage.

sets of samples were selected, each including soil samples from 0 d and 80 d of the flooding stage as well as 95 d of the drainage stage. These samples were characterized for nanoscale morphology and elemental distribution of the soil colloids using transmission electron microscopy (TEM, Talos f200x, U.S.A.) and energy-dispersive X-ray spectroscopy (EDS) mapping. The plant samples (roots, straws, and grains) were dried at 60 ℃ for 48 h and digested in a 15 mL mixture of $HClO_4$ and HNO_3 (1:4, v/v) at 120 ℃.

2.4. Statistical analysis and kinetic modeling

All statistical analyses were conducted using SPSS 22.0 (IBM Corporation, Armonk, New York, U.S.A.). Kinetic experimental data were matched by Kintek Explorer 8.0 (Johnson et al., 2009). In the kinetic model, reactive organic carbon (ROC) comprised humic acid (82 %) and fulvic acid (18 %) (Shi et al., 2013). Total surface sites concentrations for ROC were obtained by Stockholm humic model (Gustafsson and Berggren Kleja, 2005). Cr bioaccumulation factor from soil to root ($BCF_{soil\text{-}root}$) and soil to grain ($BCF_{soil\text{-}grain}$) were calculated as:

$$BCF_{soil\text{ - }root} = C_{root}/\ C_{soil} \quad (1)$$

$$BCF_{soil\text{ - }grain} = C_{grain}/\ C_{soil} \quad (2)$$

Cr translocation factor from root to straw ($TF_{root\text{-}straw}$) and shoot to grain ($TF_{straw\text{-}grain}$) were calculated as:

$$TF_{root\text{ - }straw} = C_{straw}/\ C_{root} \quad (3)$$

$$TF_{grain\text{ - }straw} = C_{grain}/\ C_{straw} \quad (4)$$

Where C_{grain}, C_{straw}, C_{root}, and C_{soil} are the Cr concentrations of grain, straw, root, and soil, respectively.

3. Results

3.1. Fluctuation of soil redox conditions and associated chemical dynamics

During flooding, the soil Eh value, an indicator of redox oscillation, rapidly decreased from 236 mV to −119 mV within the first 7 d and gradually decreased to −258 mV from 7 to 80 d. This indicates that reducing conditions lasted throughout the flooding stage (Fig. 1a). Conversely, the soil Eh value rapidly increased to 216 mV during drainage, indicating a rapid restoration of the oxidative environment (Fig. 1a). The soil pH value increased from 5.7 to 6.6 on 80 d during flooding (Fig. 1b). This increase was likely caused by proton consumption during the reduction of nitrate, sulfate, and Fe(III) (Huang et al., 2023). During drainage, soil pH decreased from 6.6 to 5.5 on 95 d (Fig. 1b).

The concentrations of $Fe(II)_{dissolved}$ and $Fe(II)_{HCl}$ increased during flooding, reaching 63.8 mg/kg for $Fe(II)_{dissolved}$ and 36.5 g/kg for $Fe(II)_{HCl}$, respectively by 80 d. (Figs. 2a and b). The concentration of $Fe(III)_{HCl}$ decreased from 16.0 g/kg to 2.4 g/kg, indicating Fe(III) reduction during this stage (Fig. 2b). Following an increase in Eh value, the concentrations of $Fe(II)_{dissolved}$ and $Fe(II)_{HCl}$ rapidly decreased between 80 d and 95 d during drainage (Figs. 2a and b). The concentration of $Fe(III)_{HCl}$ increased from 2.4 g/kg to 25.9 g/kg (Fig. 2b), suggesting Fe(II) oxidation during drainage.

The concentrations of nitrate exhibited a rapid decline from 18.2 mg/kg to 3.9 mg/kg during flooding, and slightly increased to 4.9 mg/kg during drainage (Fig. 2c). Similarly, sulfate concentrations markedly decreased from 33.2 mg/kg to 0 mg/kg due to the reduction of sulfate during flooding, and increased significantly after drainage, indicating that sulfides were oxidized to sulfate (Fig. 2c). Fig. 2d shows the changes in DOC concentrations throughout the flooding–drainage cycle. DOC concentrations increased pronouncedly from 18.2 mg/kg to 43.9 mg/kg during flooding, and then declined to 9.3 mg/kg during drainage.

3.2. Cr mobilization and fractional transformation

Basalt-derived paddy soil contained 288 mg/kg Cr, significantly exceeding the average concentration of Cr in paddy soils (59.5 mg/kg) (Kabata-Pendias, 2000). The concentration of dissolved Cr (F0) increased from 16 μg/kg to 47 μg/kg during flooding, whereas it decreased to 22 μg/kg during drainage (Fig. 5a). The Cr concentrations of F1 and F2 increased from 57 μg/kg to 79 μg/kg and 2.0 mg/kg to 2.9 mg/kg, respectively, during the flooding stage. They decreased to 39 μg/kg and 1.4 mg/kg, respectively during the drainage stage (Figs. 5b and c).

The concentration of F3 exhibited relative stability during flooding, whereas it slightly increased from 13.8 mg/kg to 15.0 mg/kg during drainage (Fig. 5d). The concentration of F4 increased to 35.2 mg/kg during the flooding stage, and decreased to 23.7 mg/kg during the drainage stage (Fig. 5e). F5 was the predominant fraction, with its concentration gradually decreasing from 243.2 mg/kg to 236.1 mg/kg during flooding, and then increasing to 247.9 mg/kg during drainage (Fig. 5f).

3.3. Soil physical property alterations

The absorbance values of the supernatant on 80 d were markedly higher than those on 0 d or 95 d, indicating an increase of colloid release during flooding and a decrease during drainage (Fig. 4a). Changes in soil pore size distribution throughout the flooding–drainage cycle were shown in Fig. 4b. On 0 d and 95 d, the soil porosity was dominated by large aperture (>100 μm), while on 80 d, the soil showed a notable increase in the volume of micropores (30–5 μm), mesopores (75–30 μm), and macropores (100–75 μm). The H_s values significantly increased from 0.078 mol/kg to 0.14 mol/kg during flooding, whereas H_s values significantly decreased to 0.075 mol/kg during drainage (Fig. 4c).

The nanoscale morphology and elemental distribution of Fe, C, oxygen (O), and aluminum (Al) of the colloids were characterized using the HAADF-TEM images and EDS mapping (Fig. 5, Fig. S1). An even distribution of Fe in soil particles on 80 d during flooding was observed while Fe appeared strongly agglomerated and unevenly distributed in the soil particles on 0 d during flooding and 95 d during drainage. The Fe signal of EDS line scans markedly fluctuated on 0 d during flooding and 95 d during drainage (Figs. 5a and c). In contrast, Fe was more dispersed and evenly distributed in the soil particles on 80 d during flooding, and the Fe signal of EDS line scans was relatively flat (Fig. 5b). This pattern indicated a clear sequence of Fe (oxyhydr)oxides dispersion and reaggregation, primarily driven by Fe (oxyhydr)oxides reduction during flooding and subsequent Fe(II) oxidation during drainage. The distribution of Cr was not detected, as its concentration was below the detection limit of EDS mapping.

3.4. Cr uptake, translocation, and accumulation in rice plants

The Cr concentrations of the roots, straws, and rice grains were 13.6–25.9 mg/kg, 5.3–12.9 mg/kg, and 0.6–2.0 mg/kg, respectively (Fig. 6a). Cr distribution in rice plant tissues followed the order of roots > straws > rice grains, which is consistent with a previous study of other plants (Singh et al., 2013). Cr concentration of roots pronouncedly decreased from 7 to 60 d during flooding (Fig. 6a). The high Cr concentration of roots on 7 d may be due to the relatively small root biomass (0.03 g) and the rapid uptake of Cr. With the increase of root biomass to 2.65 g and the decrease of Cr uptake rate, the Cr concentration in rice root decreased from 7 to 60 d (Fig. 6a, Fig. S2). From 60 to 80 d during flooding and 80 to 95 d during drainage, the Cr concentrations of roots remained relatively stable (Fig. 6a). These results are likely attributable to the dynamic equilibrium between the Cr uptake from soil to root, Cr translocation from root to straw, and the growth of biomass.

A BCF value of less than 1 indicates that the plant absorbs heavy metals without substantial accumulation, whereas a BCF value greater

than 1 indicates the capacity of plant to accumulate metals (Liu et al., 2009). In this study, the values of $BCF_{soil\text{-}root}$ of 0.047 to 0.090 (Fig. 6b) were slightly higher than the $BCF_{soil\text{-}root}$ value (0.035——0.050) in the paddy soil with the Cr concentration from 50.2 to 67.5 in a previous study (Liu et al., 2007). The $BCF_{soil\text{-}root}$ values of Cr are much lower than those of arsenic (As) (3.00——3.76), cadmium (Cd) (0.97——44.13), and mercury (Hg) (0.86——3.9) (Liu et al., 2007).

Cr concentration of straws decreased from 30 to 60 d during flooding, and remained relatively stable on 60 to 80 d during flooding and 80 to 95 d during drainage (Fig. 6a). Cr is a non-essential element, and rice plants lack specific transporters or channels for Cr uptake (Li et al., 2024). The carriers of Fe (e.g., OsYSL15) may be responsible for Cr uptake in rice plants (Li et al., 2024). The values of $TF_{root\text{-}straw}$ and $TF_{straw\text{-}grain}$ were from 0.38 to 0.64 and 0.08 to 0.34 (Fig. 6c). The observation that $TF_{root\text{-}straw}$ and $TF_{straw\text{-}grain}$ were higher than $BCF_{soil\text{-}root}$ suggests that the transformation from soil to root is the critical step in Cr accumulation in rice. Cr uptake from soil into the root system appears to be the rate-limiting process, whereas the subsequent translocation from root to aboveground tissues is comparatively more efficient.

Cr concentration in rice grains markedly increased from 0.6 mg/kg to 2.0 mg/kg during flooding. At harvest, Cr concentration in rice grains was 1.6 mg/kg on 95 d during drainage, still exceeding the safety threshold of 1 mg/kg. These results indicate high Cr mobility and availability, and a potential high health risk in basalt-derived soils of this study (Fig. 6a). The values of $BCF_{soil\text{-}grain}$ ranged from 0.0021 to 0.0068 (Fig. 6b), which were similar to the $BCF_{soil\text{-}grain}$ value (0.0028——0.0065) of Cr in a previous study (Liu et al., 2007).

4. Discussion

4.1. Effect of Fe-C-N-S cycling on Cr availability

Available Cr (sum of fractions F0, F1, and F2) was positively correlated with the concentration of $Fe(II)_{dissolved}$ ($R = 0.934$, $P < 0.01$), $Fe(II)_{HCl}$ ($R = 0.944$, $P < 0.01$), $Fe(III)_{HCl}$ ($R = -0.923$, $P < 0.01$) and DOC ($R = 0.983$, $P < 0.01$). In contrast, available Cr was not significantly correlated with nitrate ($R = -0.075$, $P = 0.872$) and sulfate concentrations ($R = -0.285$, $P = 0.536$) (Fig. S3). These results suggest that available Cr was released through Fe(III) reduction during flooding. Cr was adsorbed onto secondary Fe minerals or physical encapsulation within the amorphous or microcrystalline Fe (oxyhydr)oxides through Fe(II) oxidation during drainage (Hu et al., 2024). The concentrations of DOC increase through three mechanisms during flooding: (1) desorption of organic carbon (OC) from the surface of minerals and soil particles with the increase in pH (Zhang et al., 2024); (2) release of OC upon microbial or abiotic Fe (oxyhydr)oxides reduction (Dong et al., 2022); (3) release of OC from root exudates, primarily consisting of low molecular weight compounds (e.g., simple carbohydrates, amino acids, and organic acids) (Ge et al., 2012). DOC can act as an electron shuttle with redox-active quinone groups, facilitating electron transfer between Fe (oxyhydr)oxides and Fe-reducing bacteria, and serving as a carbon source and an electron donor for microbial activity (Dong et al., 2023). Thus, DOC release promoted microbial Fe(III) reduction during flooding, consequently leading to Cr release (Hu et al., 2023). The pH during the flooding–drainage cycle remained above 5.5, a condition under which dissolved Cr(III) can readily precipitate as $Cr(OH)_3$. Nevertheless, dissolved Cr was still detected in the soil solution at pH 6.6 (80 d of flooding), which is likely attributable to the formation of soluble DOC-Cr (III) complexes.

Fe(III) reduction triggered Cr release during flooding, whereas Fe(II)-catalyzed recrystallization induced dissolved Cr incorporation into the crystal lattice of secondary Fe mineral (Handler et al., 2014). Thus, the relative stability of F3 during flooding may result from the dynamic balance between the reduction and recrystallization of Fe (oxyhydr) oxides. The concentration of F4 increased during flooding, and decreased during drainage (Fig. 5e). The rapid increase in pH value enhanced complexation between Cr and OM during flooding, increasing OM-bound Cr. Additionally, the reduction of sulfate may result in the formation of Cr sulfide during flooding (Armienta et al., 1996; Zawadzka et al., 2007). During the drainage stage, the decrease in pH increased the adsorption of DOC onto soil surfaces and secondary Fe minerals (Duan et al., 2023), leading to a rapid decrease in DOC levels. Additionally, the complexation between OM and Cr was likely diminished by the lower pH. The oxidation of sulfide may induce a decline of F4 concentrations. The decrease of F5 concentration during flooding indicates that residual Cr was transformed into more mobile fractions (e.g., F3 and F4) during the breakdown of soil aggregates and reductive dissolution of Fe minerals. During the drainage stage, the increase of F5 concentration suggests that part of the more mobile fractions was transformed into this residual pool through processes such as Fe(II) oxidation.

In this study, Cr(VI) was not detected in any soil fraction throughout the flooding–drainage cycle. This observation is consistent with the basalt-derived geogenic origin of Cr in these soils. Cr in basalt-derived soils mainly originates from chromite and Cr-bearing minerals such as pyroxenes, predominantly as Cr(III) (Sun et al., 2022). Under flooded conditions, the strongly reducing environment rapidly converts any potentially trace Cr(VI) to Cr(III). During drainage, the oxidation of Cr (III) to Cr(VI) relies primarily on high-valent manganese (Mn) oxides (e.g., MnO_2). However, although redox potential increases, the regeneration of reactive Mn oxides is often limited or passivated (Aiken et al., 2023). Mn oxides are readily reduced and dissolved during flooding, decreasing their availability. Newly formed Mn oxides may be of low crystallinity or coated by OM, which further reduces their oxidative capacity (Aiken et al., 2023). As a result, the oxidation of Cr(III) is strongly suppressed (Aiken et al., 2023).

Table 2
Reactions and rate constants during the flooding stage in basalt-derived paddy soil.

No.	Reactions	Rate constants	Units
The flooding stage			
Fe-C-N-S cycling			
R1	$Fe(III) \rightarrow Fe(II)$	$k_1 = 0.037$	d^{-1}
R2	$ROC \rightarrow DOC$	$k_2 = 1.8 \times 10^{-5}$	d^{-1}
R3	$NO_3^- \rightarrow NO_2^-$	$k_3 = 0.014$	d^{-1}
R4	$SO_4^{2-} \rightarrow S^{2-}$	$k_4 = 0.059$	d^{-1}
R5	$\Delta Sites \rightarrow Sites_{increase}$	$k_5 = 0.057$	d^{-1}
The transformation of Cr species			
R6	$Cr_{F5} \rightarrow Cr_{F3}$	$k_6 = 7.0 \times 10^{-5}$	d^{-1}
R7	$Cr_{F5} \rightarrow Cr_{F4}$	$k_7 = 3.3 \times 10^{-4}$	d^{-1}
R8	$Cr_{F3} \rightarrow Cr_{F1+2}$	$k_8 = 1.3 \times 10^{-3}$	d^{-1}
R9	$Cr_{F4} \rightarrow Cr_{F1+2}$	$k_9 = 2.2 \times 10^{-6}$	d^{-1}
R10	$Cr_{F1+2} + Sites_{DOC} \rightarrow Cr_{F0}$	$k_{10} = 5.6 \times 10^{-5}$	$\mu mol^{-1}\ kg\ d^{-1}$
R11	$Cr_{F1+2} + Sites_{increase} \rightarrow Cr_{F3}$	$k_{11} = 8.8 \times 10^{-11}$	$\mu mol^{-1}\ kg\ d^{-1}$
R12	$Cr_{F1+2} + Sites_{increase} \rightarrow Cr_{F4}$	$k_{12} = 7.5 \times 10^{-8}$	$\mu mol^{-1}\ kg\ d^{-1}$
R13	$Cr_{F0} + Sites_{increase} \rightarrow Cr_{F3}$	$k_{13} = 2.6 \times 10^{-9}$	$\mu mol^{-1}\ kg\ d^{-1}$
R14	$Cr_{F0} + Sites_{increase} \rightarrow Cr_{F4}$	$k_{14} = 4.7 \times 10^{-10}$	$\mu mol^{-1}\ kg\ d^{-1}$

4.2. Influence of soil physical properties on Cr dynamics

Soil physical properties strongly influence Cr mobilization and sequestration. Prolonged flooding led to the breakdown of soil aggregates, resulting in an increase in micropores and mesopores as well as higher H_s. These changes enhanced the dispersion of metastable Fe (oxyhydr)oxides, and consequently facilitated the release of Fe-associated Cr into porewater. The elevated H_s during flooding also provided more reactive sites for DOC-Cr complexation, further contributing to Cr mobilization.

In contrast, during drainage, Fe(II) oxidation promoted the re-aggregation of soil particles, accompanied by a reduction in micropores and H_s. This physical reorganization reduced the number of available binding sites for DOC-Cr complexes and favored the occlusion or co-precipitation of Cr within re-formed Fe (oxyhydr)oxides. The

Table 3
Reactions and rate constants during the drainage stage in basalt-derived paddy soil.

No.	Reactions	Rate constants	Units
The drainage stage			
Fe-C-N-S cycling			
R15	$Fe(II) \rightarrow Fe(III)$	$k_{15} = 0.23$	d^{-1}
R16	$Fe(III) \rightarrow Fe(OH)_3$	$k_{16} = 9.0 \times 10^{-3}$	d^{-1}
R17	$DOC \rightarrow ROC$	$k_{17} = 0.094$	d^{-1}
R18	$NO_2^- \rightarrow NO_3^-$	$k_{18} = 0.092$	d^{-1}
R19	$S^{2-} \rightarrow SO_4^{2-}$	$k_{19} = 0.021$	d^{-1}
R20	$\Delta Sites \rightarrow Sites_{decrease}$	$k_{20} = 0.14$	d^{-1}
The transformation of Cr species			
R21	$Cr_{F0+F1+F2} + Sites_{decrease} \rightarrow Cr_{F3}$	$k_{18} = 9.2 \times 10^{-7}$	$\mu mol^{-1}\ kg\ d^{-1}$
R22	$Cr_{F0+F1+F2} + Sites_{decrease} \rightarrow Cr_{F4}$	$K_{19} = 3.0 \times 10^{-7}$	$\mu mol^{-1}\ kg\ d^{-1}$
R23	$Cr_{F0+F1+F2} + Sites_{decrease} \rightarrow Cr_{F5}$	$k_{20} = 8.4 \times 10^{-8}$	$\mu mol^{-1}\ kg\ d^{-1}$
R24	$Cr_{F3} \rightarrow Cr_{F0+1+2}$	$k_{21} = 6.5 \times 10^{-7}$	d^{-1}
R25	$Cr_{F4} \rightarrow Cr_{F0+1+2}$	$k_{22} = 3.9 \times 10^{-5}$	d^{-1}
R26	$Cr_{F3} + Sites_{decrease} \rightarrow Cr_{F5}$	$k_{23} = 1.5 \times 10^{-8}$	$\mu mol^{-1}\ kg\ d^{-1}$
R27	$Cr_{F4} + Sites_{decrease} \rightarrow Cr_{F5}$	$k_{24} = 1.2 \times 10^{-6}$	$\mu mol^{-1}\ kg\ d^{-1}$

increase in residual Cr during drainage supports this interpretation, as it indicates the gradual transfer of Cr into less mobile pools through both chemical and physical encapsulation. These findings underscore that physical processes such as aggregate stability, pore structure evolution, and surface site availability play important roles in Cr dynamics.

4.3. Quantitative insights into the contributions of Fe (oxyhydr)oxides and OM to Cr transformation

A process-based kinetic model was developed to quantitatively describe the key reactions through flooding and drainage alterations, based on the changes in soil physicochemical characteristics and Cr fractions. In this study, the concentration of Mn (0.45 g/kg) was much lower than that of Fe (86.5 g/kg) (Table 1), indicating that Fe–Mn oxide-bound Cr was predominantly associated with Fe (oxyhydr)oxides.

During the flooding stage, the processes related to Fe-C-N-S cycling included (Table 2): (i) reduction of Fe (oxyhydr)oxides primarily driven by microorganisms (R1); (ii) release of DOC from reactive organic carbon (ROC) (R2); (iii) reduction of nitrate to nitrite and sulfate to sulfite (R3 and R4); (iv) the increase in H_s (R5). Soil aggregates were broken down. The rapid decrease in Eh caused the reduction of Fe (oxyhydr) oxides, sulfate, and nitrate (Lu et al., 2023). As a result, larger amounts of protons were utilized, resulting in an increase in pH. Consequently, the values of H_s and the effective binding sites increased (Lu et al., 2023). The processes related to Cr transformation included (Table 2): (i) transformation of residual Cr to Fe (oxyhydr)oxides-bound Cr and OM-sulfide-bound Cr, respectively (R6 and R7). The reductive dissolution of Fe (oxyhydr)oxides and the breakdown of soil aggregates led to the partial destabilization of the residual Cr. As a result, a fraction of residual Cr may be redistributed into more labile pools, including Fe (oxyhydr)oxides-bound Cr and OM-sulfide-bound Cr. (ii) Fe (oxyhydr) oxides-bound Cr and OM-sulfide-bound Cr were further transferred to exchangeable Cr (F1) and specifically adsorbed Cr (F2) (R8 and R9). Residual Cr is an unextractable fraction, and F1 and F2 cannot be directly released from residual Cr (Tessier et al., 1979). (iii) transformation of F1 and F2 to dissolved Cr (F0) through the formation of soluble DOC-Cr(III) complexes (R10). DOC was released via Fe (oxyhydr)oxides reduction and root exudates. (iv) transformation of F0, F1, and F2 into Fe (oxyhydr)oxides-bound Cr through re-adsorption by Fe (oxyhydr)oxides (R11 and R13). (v) immobilization of F0, F1, and F2 through re-adsorption by OM (R12) and the formation of Cr sulfide (R14).

During the drainage stage, the processes related to Fe-C-N-S cycling were reversed, including (Table 3): (i) Fe(II) oxidation and Fe(III) hydrolysis to form $Fe(OH)_3$ (R15 and R16); (ii) conversion of DOC into ROC (R17); (iii) nitrite and sulfide oxidation (R18 and R19); (iv)

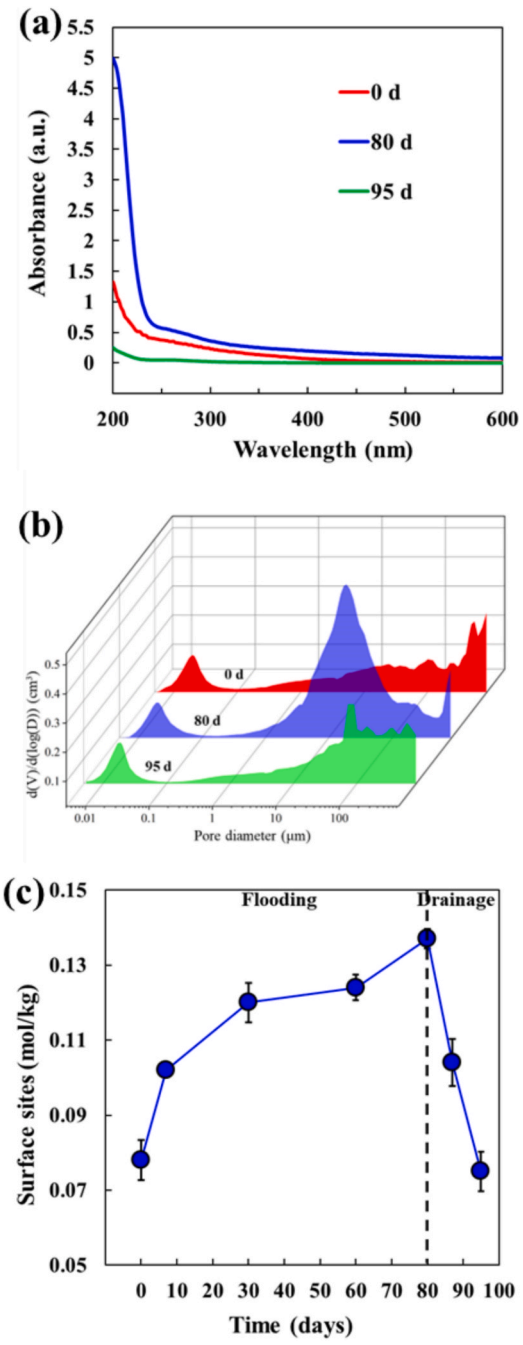

Fig. 3. UV–vis spectra of supernatant (200 to 600 nm) (a), differential pore size distribution of soil samples (b), and concentrations of surface sites (H_s) (c) throughout the flooding and drainage cycle. The dashed line indicates the transition from flooding to drainage.

decrease in H_s (R20). During drainage, the presence of O_2 caused the oxidation of Fe(II) and sulfide. Greater amounts of protons were released, leading to a decrease in pH (Chi et al., 2023). The values of H_s and the effective binding sites decreased (Chi et al., 2023). The processes related to Cr transformation included (Table 3): (i) conversion of dissolved, exchangeable, and specifically adsorbed Cr (available Cr) into Fe (oxyhydr)oxides-bound Cr, OM-sulfide-bound Cr, and residual Cr (R21, R22, and R23); (ii) conversion of available Cr into residual Cr (R23), representing the incorporation of available Cr into the crystal lattice of Fe (oxyhydr)oxides; (iii) part of Fe (oxyhydr)oxides-bound Cr was transferred back to available Cr via desorption from Fe (oxyhydr)oxides (R24); (iv) part of OM-sulfide-bound Cr was transferred back to

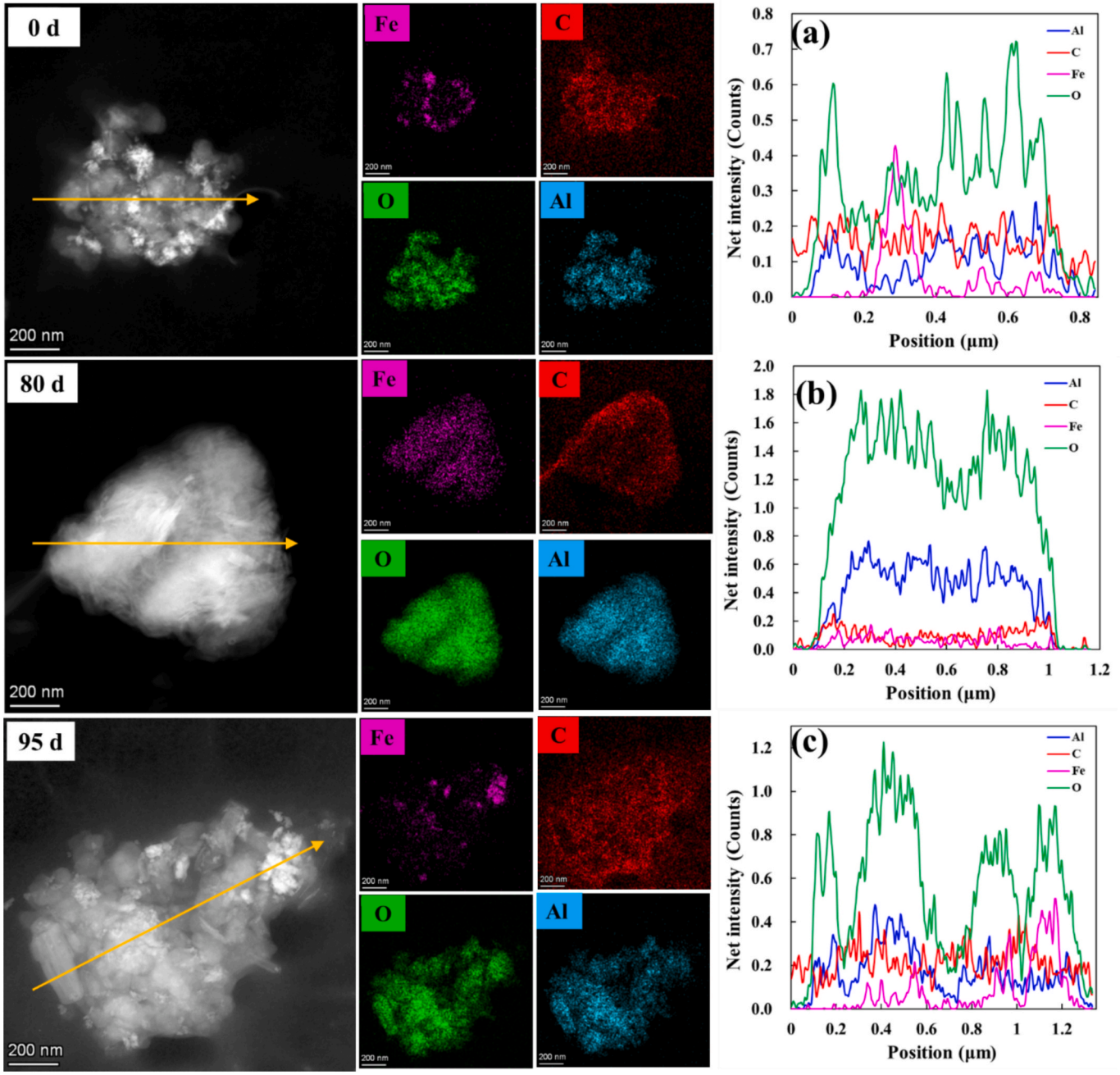

Fig. 4. Representative transmission electron microscopy with the high-angle annular detector dark-field (HAADF-TEM) images of soil particles, energy-dispersive X-ray spectroscopy (EDS) mapping, and EDS line scans of Fe, C, O, and Al distributions on Fe-bearing minerals at (a) 0 d of flooding, (b) 80 d of flooding, and (c) 95 d of drainage.

available Cr through desorption from OM and oxidation of Cr sulfide (R25); (v) conversion of Fe (oxyhydr)oxides-bound Cr and OM-sulfide-bound Cr to residual Cr (R26 and R27). It is important to note that the residual fraction (F5) in the Tessier scheme represents lattice-incorporated Cr hosted in primary silicates or highly crystalline oxides. However, under short-term redox fluctuations, the conversion of F3 and F4 to F5 (R26 and R27) primarily resulted from the strong occlusion of Cr within newly formed crystalline Fe (oxyhydr)oxides, which are co-extracted during the operational residual fraction step, rather than from lattice incorporation. A kinetic model for Cr transformation throughout the flooding–drainage cycle was developed via R1–R27. The values of k_1 to k_{27} denote the rate constants of R1–R27 (Table 2; Table 3). By fitting the observed kinetics of Cr species, $Fe(III)_{HCl}$, $Fe(II)_{HCl}$, sulfate, nitrate, and DOC throughout the flooding–drainage cycle (Fig. 2, Fig. 3c, and Fig. 5), the model-derived k values were quantified (Fig. 7). The upper and lower limits of k_1–k_5 and k_{12}–k_{17} during Fe-C-N-S cycling were obtained using a threshold of 0.95 (Table S2, Fig. S4). Because the elementary reaction equations of Cr transformation are overly complex, the upper and lower limits of k values during Cr transformation could not be determined using Kintek Explorer 8.0. Model-derived kinetic variations of different Cr fractions throughout the flooding and drainage cycle are provided in Fig. S5. The quantitative contributions of (i) Fe (oxyhydr)oxides and OM to Cr mobilization during flooding via Eq. 5–6, and (ii) metastable, stable Fe (oxyhydr)oxides, and OM to Cr

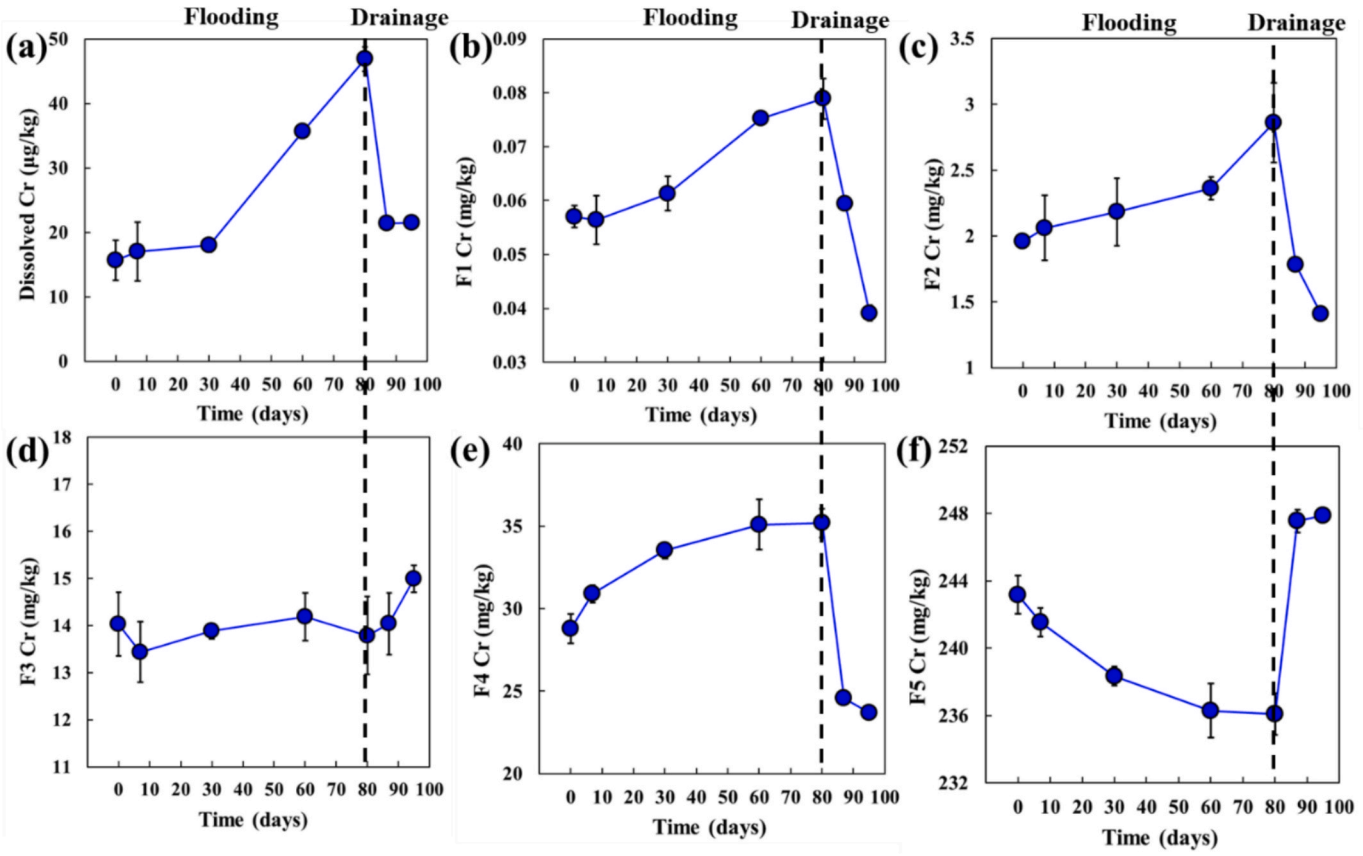

Fig. 5. Changes in dissolved Cr (F0) (a) and Cr fractions determined by the five-step sequential extraction method throughout the flooding and drainage cycle: Exchangeable Cr (F1) (b), carbonate-bound Cr (F2) (c), Fe–Mn oxide-bound Cr (F3) (d), organic-sulfide-bound Cr (F4) (e), and residual Cr (F5) (f). The dashed line indicates the transition from flooding to drainage.

sequestration during drainage were calculated via Eq. 7–9:

Cr mobilization during flooding

$$\%(Fe) = \frac{k_8[Cr_{F3}] - k_{11}[Cr_{F1+2}][Sites_{increase}] - k_{13}[Cr_{F0}][Sites_{increase}]}{k_8[Cr_{F3}] - k_{11}[Cr_{F1+2}][Sites_{increase}] - k_{13}[Cr_{F0}][Sites_{increase}] + k_9[Cr_{F4}] - k_{12}[Cr_{F1+2}][Sites_{increase}] - k_{14}[Cr_{F0}][Sites_{increase}]} \times 100 \quad (5)$$

$$\%(OM) = \frac{k_9[Cr_{F4}] - k_{12}[Cr_{F1+2}][Sites_{increase}] - k_{14}[Cr_{F0}][Sites_{increase}]}{k_8[Cr_{F3}] - k_{11}[Cr_{F1+2}][Sites_{increase}] - k_{13}[Cr_{F0}][Sites_{increase}] + k_9[Cr_{F4}] - k_{12}[Cr_{F1+2}][Sites_{increase}] - k_{14}[Cr_{F0}][Sites_{increase}]} \times 100 \quad (6)$$

Cr sequestration during drainage

$$\%(metastable\,Fe) = \frac{k_{21}[Cr_{F0+1+2}][Sites_{decrease}] - k_{24}[Cr_{F3}]}{k_{21}[Cr_{F0+1+2}][Sites_{decrease}] - k_{24}[Cr_{F3}] + k_{22}[Cr_{F0+1+2}][Sites_{decrease}] - k_{25}[Cr_{F4}] + k_{23}[Cr_{F0+1+2}][Sites_{decrease}]} \times 100 \quad (7)$$

$$\%(stable\,Fe) = \frac{k_{23}[Cr_{F0+1+2}][Sites_{decrease}]}{k_{21}[Cr_{F0+1+2}][Sites_{decrease}] - k_{24}[Cr_{F3}] + k_{22}[Cr_{F0+1+2}][Sites_{decrease}] - k_{25}[Cr_{F4}] + k_{23}[Cr_{F0+1+2}][Sites_{decrease}]} \times 100 \quad (8)$$

$$\%(OM) = \frac{k_{22}[Cr_{F0+1+2}][Sites_{decrease}] - k_{25}[Cr_{F4}]}{k_{21}[Cr_{F0+1+2}][Sites_{decrease}] - k_{24}[Cr_{F3}] + k_{22}[Cr_{F0+1+2}][Sites_{decrease}] - k_{25}[Cr_{F4}] + k_{23}[Cr_{F0+1+2}][Sites_{decrease}]} \times 100 \quad (9)$$

The kinetic modeling effectively quantified Cr transformation throughout the flooding–drainage cycle. During flooding, the reductive dissolution of Fe (oxyhydr)oxides emerged as the dominant process facilitating Cr mobilization, contributing 76.4 % of the available Cr release (Fig. 8a). This process is mechanistically linked to microbial or abiotic activity, where OM was utilized as an electron donor (Dong et al.,

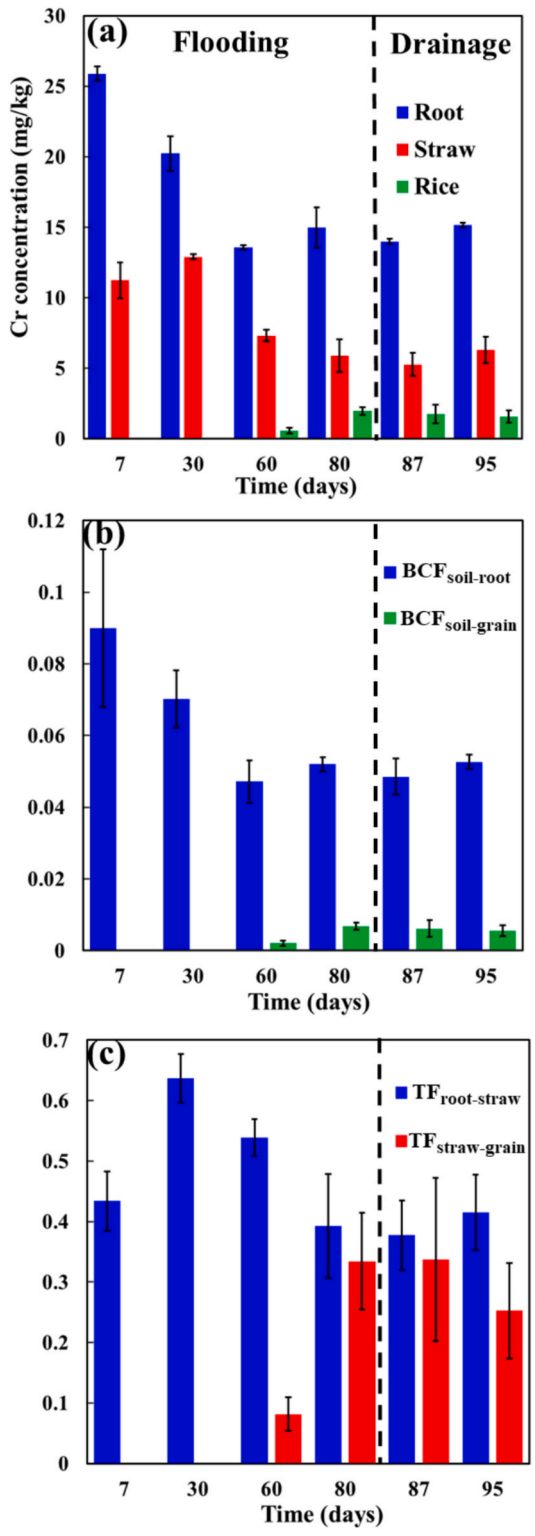

Fig. 6. (a) Concentrations of Cr in the roots, straws, rice grains throughout the flooding and drainage cycle. (b) Bioaccumulation factor from soil to root ($BCF_{soil\text{-}root}$) and from soil to grain ($BCF_{soil\text{-}grain}$). (c) Translocation factors from root to shoot ($TF_{root\text{-}straw}$) and from shoot to grain ($TF_{straw\text{-}grain}$). The dashed line indicates the transition from flooding to drainage.

2023), accelerating Fe(III) reduction and subsequent liberation of Fe (oxyhydr)oxides-bound Cr. OM played a secondary but significant role, contributing 23.6 % of the available Cr release (Fig. 8a).

During drainage, oxidative conditions triggered Fe(II) oxidation and recrystallization of metastable Fe (oxyhydr)oxides, which sequestered 76.6 % of available Cr (Fig. 8b). Metastable and stable Fe (oxyhydr) oxides contributed 91.6 % and 8.4 % to the total Fe (oxyhydr)oxides, respectively. The contribution of metastable Fe (oxyhydr)oxides indicates that the available Cr was immobilized through surface adsorption or physical encapsulation within the amorphous or microcrystalline Fe (oxyhydr)oxides, forming co-precipitates. The contribution of stable Fe (oxyhydr)oxides indicates that the available Cr was transferred into residual Cr, suggesting that Cr may incorporate into the crystal lattice of Fe (oxyhydr)oxides (Singh et al., 2002). The similar ionic radii of Cr^{3+} (0.61 Å) and Fe^{3+} (0.64 Å) facilitate the incorporation of Cr into the crystal lattice of Fe (oxyhydr)oxides (Li et al., 2025). Using EXAFS spectroscopy, Singh et al., (2002) found that up to 8 % of Fe^{3+} was replaced by Cr^{3+} in the structure of synthetic goethite. OM emerged as the second most important factor, contributing 23.1 % to the immobilization of the available Cr (Fig. 8b). OM can immobilize Cr through complexation (Ao et al., 2022). Xia et al. (2022) employed STXM-ptychography in combination with Cr K-edge XANES to examine the roles of Fe(III) minerals and DOM in Cr(III) immobilization, which was consistent with this study of kinetic modelling. The results of scanning transmission Xray microscopy (STXM) and ptychography and X-ray absorption near-edge structure (XANES) spectroscopy demonstrated that Fe (oxyhydr)oxide phases served as the dominant binding sites for Cr(III). They further showed that OM, while not the primary sorbent, indirectly enhanced Cr retention by promoting the aggregation and deposition of coprecipitates via DOM bridging or electrostatic interactions.

The strong positive correlations between available Cr and Fe(II), Fe (III), and DOC indicate that Fe and OM were the primary drivers of Cr transformation, consistent with the model outcome. Thus, while the correlation analysis provides statistical associations between variables, the kinetic model went further by quantifying process contributions and capturing their temporal evolution. Correlations highlighted key drivers observed in the data, and the model integrates these drivers into a mechanistic framework that explains their roles in Cr transformation.

4.4. Implications

This study offers important insights into the biogeochemical cycling of Cr in basalt-derived paddy soils. Cr availability is crucial for assessing Cr-related risks throughout the flooding-drainage cycle (Xiao et al., 2015). This study reveals distinct flooding- and drainage- induced shifts in Cr availability, providing valuable insights into designing effective water management strategies to regulate Cr dynamics in these soils. A previous study found that the concentrations of Cr exhibited an increase during flooding and a decrease during drainage in the porewater of floodplain meadow downstream soils (Kelly et al., 2020), which was consistent with the observed patterns of Cr availability throughout the flooding-drainage cycle in this study.

Previous kinetic studies have examined temporal fraction changes of Ni, Pb, and Cd under redox oscillations (Huang et al., 2023; Lu et al., 2023; Yang et al., 2021). The present study quantified the relative contributions of Fe (oxyhydr)oxides and OM to Cr mobilization-sequestration throughout the flooding-drainage cycle, thereby offering mechanistic insights into the processes controlling Cr mobility in soils. Furthermore, the cited studies all used soils with relatively low natural background levels of Ni, Pb, or Cd and relied on exogenous addition of these metals, which better represent contamination scenarios following accidental releases. In contrast, this study focused on basalt-derived soils with a naturally high geogenic background of Cr, which are widespread in rice-growing regions and present distinct environmental challenges. Additionally, whereas the cited studies used controlled soil microcosm systems, this study employed pot experiments. The interplay between redox oscillations, Fe (oxyhydr)oxide transformations, and OM dynamics governs Cr availability, with direct implications for soil health and agricultural sustainability. This study highlights the dual role of Fe-

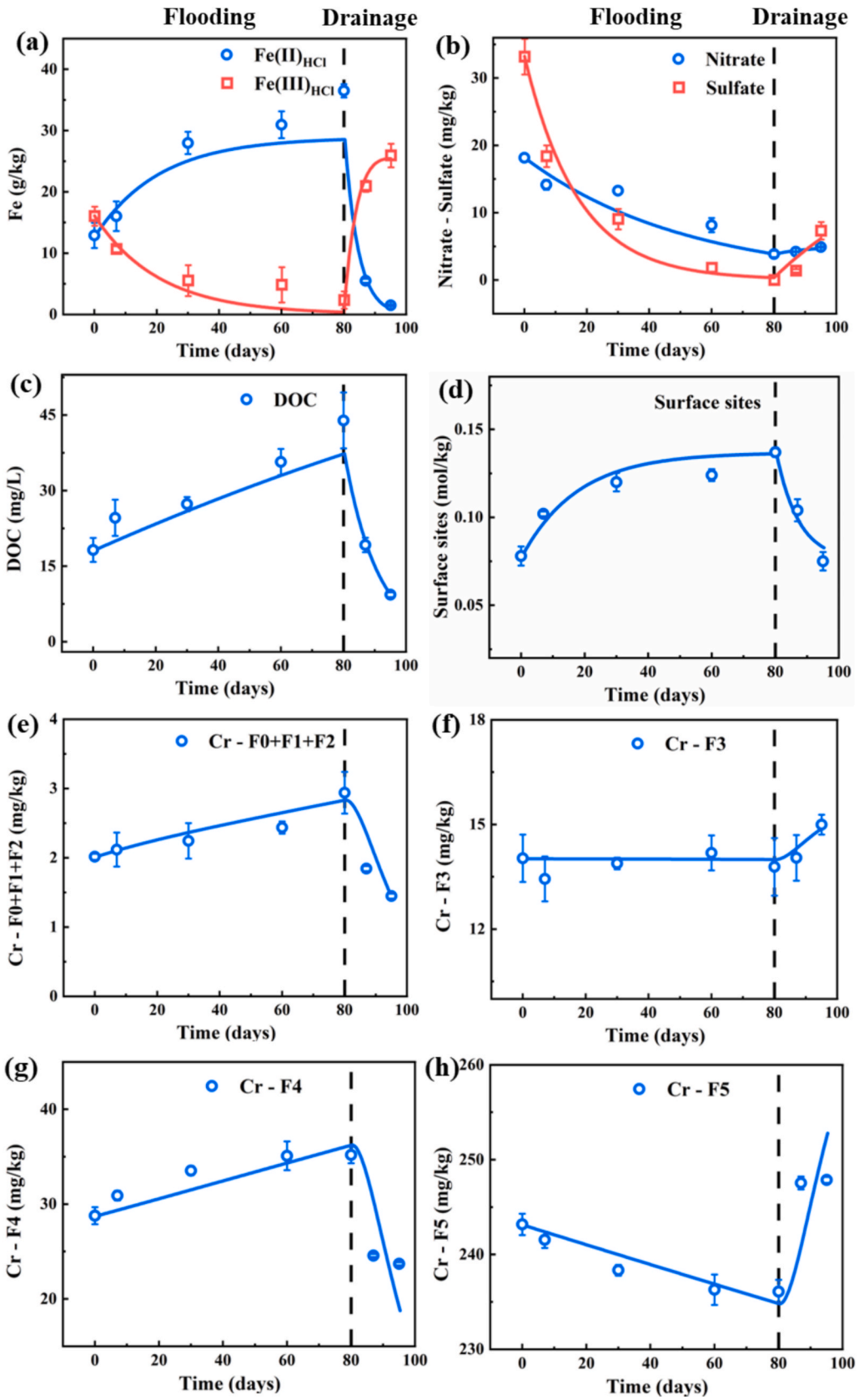

Fig. 7. Kinetic model-fitted Fe fractions (a), nitrate and sulfate (b), dissolved organic carbon (DOC) (c), concentrations of surface sites (H_s) (d), Cr fractions (F0+F1+F2) (e), Cr fraction (F3) (f), Cr fraction (F4) (g), and Cr fraction (F5) (h) throughout the flooding and drainage cycle according to reactions R1 to R27. The dashed line indicates the transition from flooding to drainage.

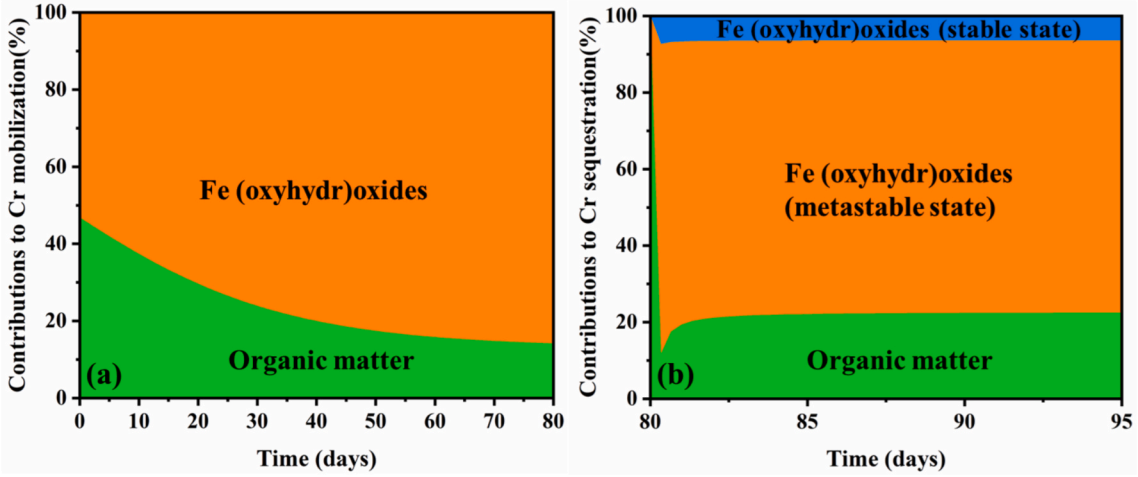

Fig. 8. Relative contributions of Fe (oxyhydr)oxides and organic matter (OM) to Cr mobilization during flooding (a), and of Fe (oxyhydr)oxides and OM to Cr sequestration during drainage (b). The contribution of metastable Fe (oxyhydr)oxides indicates that the available Cr was immobilized through adsorption on Fe (oxyhydr)oxides surfaces or physical encapsulation within Fe (oxyhydr)oxides, forming co-precipitates. The contribution of stable Fe (oxyhydr)oxides indicates that the available Cr transferred into residual Cr. The dashed line indicates the transition from flooding to drainage.

OM interactions in regulating Cr biogeochemical cycling. Optimizing flooding-drainage cycles could impact Cr mobilization pathways. Shortening the flooding duration during grain-filling stages may reduce Fe(III) reduction and DOC release, thereby limiting Cr solubility. Conversely, prolonged drainage phases could enhance Cr sequestration via Fe(II) oxidation. Fe-based amendments may promote Cr adsorption onto newly formed Fe (oxyhydr)oxides (Wang et al., 2025).

The model necessarily simplifies the highly complex interactions among Fe (oxyhydr)oxides, Cr, and OM. The fitted rate constants derived from the kinetic model are empirical and site-specific, reflecting the unique Fe, C, N, and S cycling, and Cr dynamics of the studied basalt-derived soils. These parameters cannot be directly extrapolated to other soil types. Future research should test the applicability of this modeling framework in other soil systems, such as anthropogenically contaminated soils, soils derived from different parent materials, and wetland sediments. Re-parameterization will be necessary to account for variations in soil chemical and physical properties.

5. Conclusions

Redox oscillations are widespread in the environment, including paddy soils, wetlands, and estuaries, and induce dynamic changes in the physical and chemical properties of soil. This study elucidates how Cr availability varies throughout the flooding-drainage cycle. The available Cr was released during flooding and immobilized during drainage. This study highlights the pivotal roles of Fe (oxyhydr)oxides and OM in governing Cr dynamics throughout the flooding-drainage cycle. Fe (oxyhydr)oxides dominated the available Cr mobilization (76.4 %) and sequestration (76.6 %), primarily through reductive dissolution and oxidative recrystallization. Within the Fe (oxyhydr)oxide fraction, metastable and stable Fe phases contributed 91.6 % and 8.4 % to the available Cr sequestration, respectively. OM contributed 23.6 % to the available Cr mobilization during flooding and 23.4 % to sequestration during drainage. These findings provide a mechanistic framework for managing Cr availability in paddy soils with a high geological background, emphasizing the interplay between Fe (oxyhydr)oxides and OM under redox oscillations.

CRediT authorship contribution statement

Guojun Chen: Writing – original draft, Methodology, Investigation, Formal analysis. **Yang Yang:** Writing – review & editing, Methodology. **Ke Zhang:** Investigation. **Yan Ru:** Visualization. **Zebin Hong:** Investigation. **Xiaomin Li:** Writing – review & editing. **Taicheng An:** Writing – review & editing, Funding acquisition. **Pei Wang:** Writing – review & editing. **Songxiong Zhong:** Formal analysis. **Qi Wang:** Resources. **Shiwen Hu:** Investigation. **Fangbai Li:** Writing – review & editing, Supervision. **Tongxu Liu:** Writing – review & editing, Supervision, Funding acquisition, Conceptualization.

Declaration of competing interest

The authors declare that they have no known competing financial interests or personal relationships that could have appeared to influence the work reported in this paper.

Acknowledgements

This work was funded by the National Natural Science Foundation of China (42177035, 42321005, 42261160644, and 42107338), Open-End Fund of Guangdong Key Laboratory of Environmental Catalysis and Health Risk Control (GKLECHRC-01), Youth S&T Talent Support Program of GDSTA (SKXRC2025097), Young Talent Support Project of Guangzhou Association for Science and Technology (QT-2025-022), Young Talent Project of GDAS (2023GDASQNRC-0203), GDAS' Project of Science and Technology Development (2024GDASZH-2024010102, 2022GDASZH-2022010201-04), and Guangdong Foundation for-Program of Science and Technology Research (2023B1212060044).

Appendix A. Supplementary material

Supplementary material to this article can be found online at https://doi.org/10.1016/j.gca.2025.12.050.

References

Aiken, M.L., Abernathy, M.J., Schaefer, M.V., Lee, I., Ying, S.C., 2023. Inhibition of chromium(III) oxidation through manganese(IV) oxide passivation and iron(II) abiotic reduction. ACS Earth Space Chem. 7, 2327–2338.
Ali, W., Mao, K., Zhang, H., Junaid, M., Xu, N., Rasool, A., Feng, X., Yang, Z., 2020. Comprehensive review of the basic chemical behaviours, sources, processes, and endpoints of trace element contamination in paddy soil-rice systems in rice-growing countries. J. Hazard. Mater. 397, 122720.
Ali, W., Zhang, H., Mao, K., Shafeeque, M., Aslam, M.W., Yang, X., Zhong, L., Feng, X., Podgorski, J., 2022. Chromium contamination in paddy soil-rice systems and associated human health risks in Pakistan. Sci. Total Environ. 826, 153910.
Ao, M., Chen, X., Deng, T., Sun, S., Tang, Y., Morel, J.L., Qiu, R., Wang, S., 2022. Chromium biogeochemical behaviour in soil-plant systems and remediation strategies: a critical review. J. Hazard. Mater. 424, 127233.

Armienta, M., Rodríguez, R., Ceniceros, N., Juarez, F., Cruz, O., 1996. Distribution, origin and fate of chromium in soils in Guanajuato. Mexico. Environ. Pollut. 91, 391–397.
Chen, D., Cheng, K., Liu, T., Chen, G., Kappler, A., Li, X., Zeng, R.J., Yang, Y., Yue, F., Hu, S., Cao, F., Li, F., 2023. Novel insight into microbially mediated nitrate-reducing Fe(II) oxidation by *Acidovorax* sp. strain BoFeN1 using dual N–O isotope fractionation. Environ. Sci. Technol. 57, 12546–12555.
Chen, G., Han, J., Mu, Y., Yu, H., Qin, L., 2019a. Two-stage chromium isotope fractionation during microbial Cr(VI) reduction. Water Res. 148, 10–18.
Chen, G., Bai, Y., Zeng, R.J., Qin, L., 2019b. Effects of different metabolic pathways and environmental parameters on Cr isotope fractionation during Cr(VI) reduction by extremely thermophilic bacteria. Geochim. Cosmochim. Acta 256, 135–146.
Chen, G., Zhao, W., Yang, Y., Chen, D., Wang, Y., Li, F., Zhao, Z., Cao, F., Liu, T., 2021. Chemodenitrification by Fe(II) and nitrite: Effects of temperature and dual NO isotope fractionation. Chem. Geol. 575, 120258.
Chi, W., Chen, G., Hu, S., Li, X., Cheng, K., Wang, Q., Xia, B., Yang, Y., Ma, Y., Liu, T., 2023. A small extent of seawater intrusion significantly enhanced Cd uptake by rice in coastal paddy fields. J. Hazard. Mater. 458, 131945.
Davranche, M., Bollinger, J.C., 2000. Release of metals from iron oxyhydroxides under reductive conditions: effect of metal/solid interactions. J. Colloid Interf. Sci. 232, 165–173.
Dong, H., Huang, L., Zhao, L., Zeng, Q., Liu, X., Sheng, Y., Shi, L., Wu, G., Jiang, H., Li, F., Zhang, L., Guo, D., Li, G., Hou, W., Chen, H., 2022. A critical review of mineral–microbe interaction and co-evolution: mechanisms and applications. Nat. Sci, Rev, p. 9.
Dong, H., Zeng, Q., Sheng, Y., Chen, C., Yu, G., Kappler, A., 2023. Coupled iron cycling and organic matter transformation across redox interfaces. Nat. Rev. Earth Environ. 4, 659–673.
Duan, X., Li, Z., Li, Y., Yuan, H., Gao, W., Chen, X., Ge, T., Wu, J., Zhu, Z., 2023. Iron–organic carbon associations stimulate carbon accumulation in paddy soils by decreasing soil organic carbon priming. Soil Biol. and Biochem. 179, 108972.
Ertani, A., Mietto, A., Borin, M., Nardi, S., 2017. Chromium in agricultural soils and crops: a review. Water Air Soil Pollut. 228, 190.
Ge, T., Yuan, H., Zhu, H., Wu, X., Nie, S.a., Liu, C., Tong, C., Wu, J., Brookes, P., 2012. Biological carbon assimilation and dynamics in a flooded rice–soil system. Soil Biol. and Biochem. 48, 39-46.
Gustafsson, J.P., Berggren Kleja, D., 2005. Modeling salt-dependent proton binding by organic soils with the NICA-donnan and stockholm humic models. Environ. Sci. Technol. 39, 5372–5377.
Handler, R.M., Frierdich, A.J., Johnson, C.M., Rosso, K.M., Beard, B.L., Wang, C., Latta, D.E., Neumann, A., Pasakarnis, T., Premaratne, W.A.P.J., Scherer, M.M., 2014. Fe(II)-catalyzed recrystallization of goethite revisited. Environ. Sci. Technol. 48, 11302–11311.
Huang, K., Yang, Y., Lu, H., Hu, S., Chen, G., Du, Y., Liu, T., Li, X., Li, F., 2023. Transformation kinetics of exogenous nickel in a paddy soil during anoxic-oxic alteration: Roles of organic matter and iron oxides. J. Hazard. Mater. 452, 131246.
Hu, D., Zeng, Q., Liu, X., Hu, J., Guo, D., Dong, H., 2023. Ligand enhanced bio-oxidation of structural Fe(II) in illite coupled with nitrate reduction. Geochim. Cosmochim. Acta 357, 50–63.
Hu, S., Wang, Q., Zhang, H., Yang, Y., Chen, G., Wang, S., Liu, C., Liu, T., 2024. Reduction and transformation of Cr(VI)-associated ferrihydrite by *Shewanella oneidensis* MR-1: Kinetics and secondary minerals. Geochim. Cosmochim. Acta 374, 15–32.
Johnson, K.A., Simpson, Z.B., Blom, T., 2009. Global kinetic explorer: a new computer program for dynamic simulation and fitting of kinetic data. Anal. Biochem. 387, 20–29.
Kabata-Pendias, A., 2000. Trace elements in soils and plants. CRC Press.
Kelly, T.J., Hamilton, E., Watts, M.J., Ponting, J., Sizmur, T., 2020. The effect of flooding and drainage duration on the release of trace elements from floodplain soils. Environ. Toxicol. Chem. 39, 2124–2135.
Li, J., Chen, W., Xu, K., Xie, W., Qi, H., Tang, Y., Wang, S., Deng, T., Morel, J.-L., Qiu, R., 2024. Fe(III) transporter OsYSL15 may play a key role in the uptake of Cr(III) in rice (*Oryza sativa* L.). J. Hazard. Mater. 469, 133531.
Li, Z., Goût, T.L., Hu, Y., 2025. Review on formation of iron (oxyhydr)oxide nanoparticles in the environment: interactions with metals, organics and microbes. Environ. Biogeochem. Process. 1, e003.
Liu, T., Wei, R., Li, J., Xie, W., Sun, S., Deng, T., Wang, S., Tang, Y., Lin, Q., Ni, Z., Qiu, R., 2024. Fe (hydr)oxides and organic colloids mediate colloid-bound chromium mobilization in Cr(VI) contaminated paddy soil. Environ. Pollut. 363, 125045.
Liu, W.-X., Shen, L.-F., Liu, J.-W., Wang, Y.-W., Li, S.-R., 2007. Uptake of toxic heavy metals by rice (*Oryza sativa* L.) cultivated in the agricultural soil near Zhengzhou City, People's Republic of China. B. Environ. Contam. Tox. 79, 209–213.
Liu, W.X., Liu, J.W., Wu, M.Z., Li, Y., Zhao, Y., Li, S.R., 2009. Accumulation and translocation of toxic heavy metals in winter wheat (*Triticum aestivum* L.) growing in agricultural soil of Zhengzhou. B. Environ. Contam. Tox. 82, 343–347.
Liu, X., Dong, H., Zeng, Q., Yang, X., Zhang, D., 2019. Synergistic effects of reduced Nontronite and organic ligands on Cr(VI) reduction. Environ. Sci. Technol. 53, 13732–13741.
Lu, H., Yang, Y., Huang, K., Huang, G., Hu, S., Pan, D., Liu, T., Li, X., 2023. Transformation kinetics of exogenous lead in an acidic soil during anoxic-oxic alteration: Important roles of phosphorus and organic matter. Environ. Pollut. 335, 122271.
Ma, Y., Hooda, P.S., 2010. Chromium, nickel and cobalt. In: Hooda, P. (Ed.), Trace elements in soils, first ed. John Wiley & Sons Ltd, The Atrium, Southern Gate, Chichester, West Sussex, PO19 8SQ, United Kingdom, pp. 461e480.
Novak, M., Martinkova, E., Chrastny, V., Stepanova, M., Sebek, O., Andronikov, A., Curik, J., Veselovsky, F., Prechova, E., Houskova, M., 2017. The fate of Cr(VI) in contaminated aquifers 65 years after the first spillage of plating solutions: a δ^{53}Cr study at four central European sites. Catena 158, 371–380.
Ohta, A., Kagi, H., Tsuno, H., Nomura, M., Okai, T., 2012. Speciation study of Cr(VI/III) reacting with humic substances and determination of local structure of Cr binding humic substances using XAFS spectroscopy. Geochem. J. 46, 409–420.
Santos, J.V., Goranov, A.I., Bento, L.R., Oliveira, P.P.A., Pezzopane, J.R.M., Bernardi, A. C.C., de Sá, Í.P., Nogueira, A.R.A., Martin-Neto, L., Hatcher, P.G., 2024. Biogeochemistry of dissolved organic matter and inorganic solutes in soil profiles of tropical pasturelands. Soil Tillage Res. 240, 106100.
Satpathy, D., Reddy, M.V., Dhal, S.P., 2014. Risk assessment of heavy metals contamination in paddy soil, plants, and grains (*Oryza sativa* L.) at the East Coast of India. Biomed Res. Int. 2014.
Shi, Z., Di Toro, D.M., Allen, H.E., Sparks, D.L., 2013. A general model for kinetics of heavy metal adsorption and desorption on soils. Environ. Sci. Technol. 47, 3761–3767.
Singh, H.P., Mahajan, P., Kaur, S., Batish, D.R., Kohli, R.K., 2013. Chromium toxicity and tolerance in plants. Environ. Chem. Lett. 11, 229–254.
Singh, B., Sherman, D.M., Gilkes, R.J., Wells, M.A., Mosselmans, J.F.W., 2002. Incorporation of Cr, Mn and Ni into goethite (α-FeOOH): mechanism from extended X-ray absorption fine structure spectroscopy. Clay Miner. 37, 639–649.
Song, X., Wang, P., Van Zwieten, L., Bolan, N., Wang, H., Li, X., Cheng, K., Yang, Y., Wang, M., Liu, T., Li, F., 2022. Towards a better understanding of the role of Fe cycling in soil for carbon stabilization and degradation. Carbon Res. 1, 5.
Sun, S.-S., Ao, M., Geng, K.-R., Chen, J.-Q., Li, J.-J., Guan, Z.-T., Mo, B.-L., Liu, T., Yang, W.-J., Tang, Y.-T., 2022. Enrichment and speciation of chromium during basalt weathering: Insights from variably weathered profiles in the Leizhou Peninsula, South China. Sci. Total Environ. 153304.
Tessier, A., Campbell, P.G., Bisson, M., 1979. Sequential extraction procedure for the speciation of particulate trace metals. Anal. Chem. 51, 844–851.
Wang, H., Li, X., Chen, Y., Li, Z., Hedding, D.W., Nel, W., Ji, J., Chen, J., 2020. Geochemical behavior and potential health risk of heavy metals in basalt-derived agricultural soil and crops: a case study from Xuyi County, eastern China. Sci. Total Environ. 729, 139058.
Wang, L., Song, C., Jiang, X., Li, T., Wang, H., 2025. Mechanochemical synthesis of redox-active Fe-based nanocomposites for efficient Cr(VI) remediation in water and soil. Sep. Purif. Technol. 377, 134212.
Wang, W., Chen, C., Huang, X., Jiang, S., Xiong, J., Li, J., Hong, M., Zhang, J., Guan, Y., Feng, X., Tan, W., Liu, F., Ding, L.-J., Yin, H., 2024. Chromium(VI) adsorption and reduction in soils under anoxic conditions: the relative roles of iron (oxyhr)oxides, iron(II), organic matters, and microbes. Environ. Sci. Technol. 58, 18391–18403.
Wiggenhauser, M., Aucour, A.-M., Bureau, S., Campillo, S., Telouk, P., Romani, M., Ma, J.F., Landrot, G., Sarret, G., 2021. Cadmium transfer in contaminated soil-rice systems: Insights from solid-state speciation analysis and stable isotope fractionation. Environ. Pollut. 269, 115934.
Xia, X., Wang, J., Hu, Y., Liu, J., Darma, A.I., Jin, L., Han, H., He, C., Yang, J., 2022. Molecular insights into roles of dissolved organic matter in Cr(III) immobilization by coprecipitation with Fe(III) probed by STXM-Ptychography and XANES spectroscopy. Environ. Sci. Technol. 56, 2432–2442.
Xiao, W., Ye, X., Yang, X., Li, T., Zhao, S., Zhang, Q., 2015. Effects of alternating wetting and drying versus continuous flooding on chromium fate in paddy soils. Ecotox. Environ. Safe. 113, 439–445.
Xiao, W., Ye, X., Zhu, Z., Zhang, Q., Zhao, S., Chen, D., Gao, N., Hu, J., 2021. Continuous flooding stimulates root iron plaque formation and reduces chromium accumulation in rice (*Oryza sativa* L.). Sci. Total Environ. 788, 147786.
Yang, Y., Yuan, X., Chi, W.T., Wang, P., Hu, S.W., Li, F.B., Li, X.M., Liu, T.X., Sun, Y., Qin, H.L., 2021. Modelling evaluation of key cadmium transformation processes in acid paddy soil under alternating redox conditions. Chem. Geol. 581, 120409.
Yang, Y., Peng, Y., Ma, Y., Chen, G., Li, F., Liu, T., 2022. Effects of aging and reduction processes on Cr toxicity to wheat root elongation in Cr(VI) spiked soils. Environ. Pollut. 296, 118784.
Yu, H.Y., Li, F.B., Liu, C.S., Huang, W., Liu, T.X., Yu, W.M., 2016. Iron redox cycling coupled to transformation and immobilization of heavy metals: Implications for paddy rice safety in the red soil of south China. In: Sparks, D.L. (Ed.), Adv. Academic Press, Agron, pp. 279–317.
Zawadzka, A.M., Crawford, R.L., Paszczynski, A.J., 2007. Pyridine-2, 6-bis (thiocarboxylic acid) produced by *Pseudomonas stutzeri* KC reduces chromium(VI) and precipitates mercury, cadmium, lead and arsenic. Biometals 20, 145–158.
Zhang, D., Liu, X., Guo, D., Li, G., Qu, J., Dong, H., 2022. Cr(VI) reduction by Siderophore alone and in combination with reduced clay minerals. Environ. Sci. Technol. 56, 12315–12324.
Zhang, E., Wu, S., Liu, J., Li, H., Liu, X., Lu, Y., Ge, C., Zhou, D., 2024. Activated carbon as a strong DOM adsorbent mitigates antimony and arsenic release in flooded mining-impacted soils. J. Hazard. Mater. 473, 134663.